Localized Surface Plasmon Resonance Spectroscopy and Sensing

Katherine A. Willets and Richard P. Van Duyne

Department of Chemistry, Northwestern University, Evanston, Illinois 60208-3113;
email: kallie@northwestern.edu, vanduyne@northwestern.edu

Key Words

molecular plasmonics, refractive-index sensing, surface-enhanced Raman scattering, nanoparticles, nanosphere lithography

Abstract

Localized surface plasmon resonance (LSPR) spectroscopy of metallic nanoparticles is a powerful technique for chemical and biological sensing experiments. Moreover, the LSPR is responsible for the electromagnetic-field enhancement that leads to surface-enhanced Raman scattering (SERS) and other surface-enhanced spectroscopic processes. This review describes recent fundamental spectroscopic studies that reveal key relationships governing the LSPR spectral location and its sensitivity to the local environment, including nanoparticle shape and size. We also describe studies on the distance dependence of the enhanced electromagnetic field and the relationship between the plasmon resonance and the Raman excitation energy. Lastly, we introduce a new form of LSPR spectroscopy, involving the coupling between nanoparticle plasmon resonances and adsorbate molecular resonances. The results from these fundamental studies guide the design of new sensing experiments, illustrated through applications in which researchers use both LSPR wavelength-shift sensing and SERS to detect molecules of chemical and biological relevance.

INTRODUCTION

SPR: surface plasmon resonance

LSPR : localized surface plasmon resonance

Localized surface plasmon: a photon-driven coherent oscillation of the surface conduction electrons in a material with negative real and near-zero imaginary dielectric constant

SERS : surface-enhanced Raman scattering

Materials that possess a negative real and small positive imaginary dielectric constant are capable of supporting a surface plasmon resonance (SPR). This resonance is a coherent oscillation of the surface conduction electrons excited by electromagnetic (EM) radiation. Plasmonics is the study of these particular light-matter interactions, which have enabled a vast array of applications, including surface-enhanced spectroscopies (1–16), biological and chemical sensing (17–33), and lithographic fabrication (34–36). Plasmonic materials can already be found in commercial instruments, such as the BIAcore®, which monitors the thermodynamics and kinetics of biological binding processes using SPR spectroscopy (27, 29, 37). In these experiments, researchers use thin (∼50-nm) metal films as the sensing platform; these yield propagating plasmons, also known as surface plasmon polaritons (27, 38, 39). However, with recent advances that allow the controlled fabrication and manipulation of metallic structures on the nanoscale, researchers have demonstrated new applications that take advantage of the localized surface plasmon resonance (LSPR) (17, 19, 21, 22, 40–42).

Figure 1 illustrates the difference between propagating and localized surface plasmons (38, 41, 43). In the case of surface plasmon polaritons, plasmons propagate in the *x*- and *y*-directions along the metal-dielectric interface, for distances on the order of tens to hundreds of microns, and decay evanescently in the *z*-direction with 1/e decay lengths on the order of 200 nm (27, 39, 44). The interaction between the metal surface-confined EM wave and a molecular surface layer of interest leads to shifts in the plasmon resonance condition, which can be observed in three modes: (*a*) angle resolved, (*b*) wavelength shift, and (*c*) imaging (27). In the first two modes, one measures the reflectivity of light from the metal surface as a function of either angle of incidence (at constant wavelength) or wavelength (at constant angle of incidence). The third method uses light of both constant wavelength and incident angle to interrogate a two-dimensional region of the sample, mapping the reflectivity of the surface as a function of position.

For the case of localized surface plasmons, light interacts with particles much smaller than the incident wavelength (**Figure 1b**). This leads to a plasmon that oscillates locally around the nanoparticle with a frequency known as the LSPR (41, 43). Similar to the SPR, the LSPR is sensitive to changes in the local dielectric environment (43, 45, 46). Typically researchers sense changes in the local environment through an LSPR wavelength-shift measurement, although a variant of angle-resolved sensing for the LSPR is also possible (47).

Significant interest in understanding propagating and localized surface plasmons developed on the discovery of surface-enhanced Raman scattering (SERS) (1, 48). Researchers proposed competing mechanisms of both chemical and EM-field enhancements to explain the observed Raman enhancement on roughened metallic substrates (5, 49–55). Because the EM-field-enhancement mechanism required coupling of the incident radiation to the metal surface, researchers devoted much theoretical and experimental effort to understanding surface plasmons (5, 50, 56, 57). In particular, they studied the role of size, shape, material, and local dielectric properties—all of which determine the LSPR wavelength (20, 41, 43, 45, 58, 59). Whereas these studies
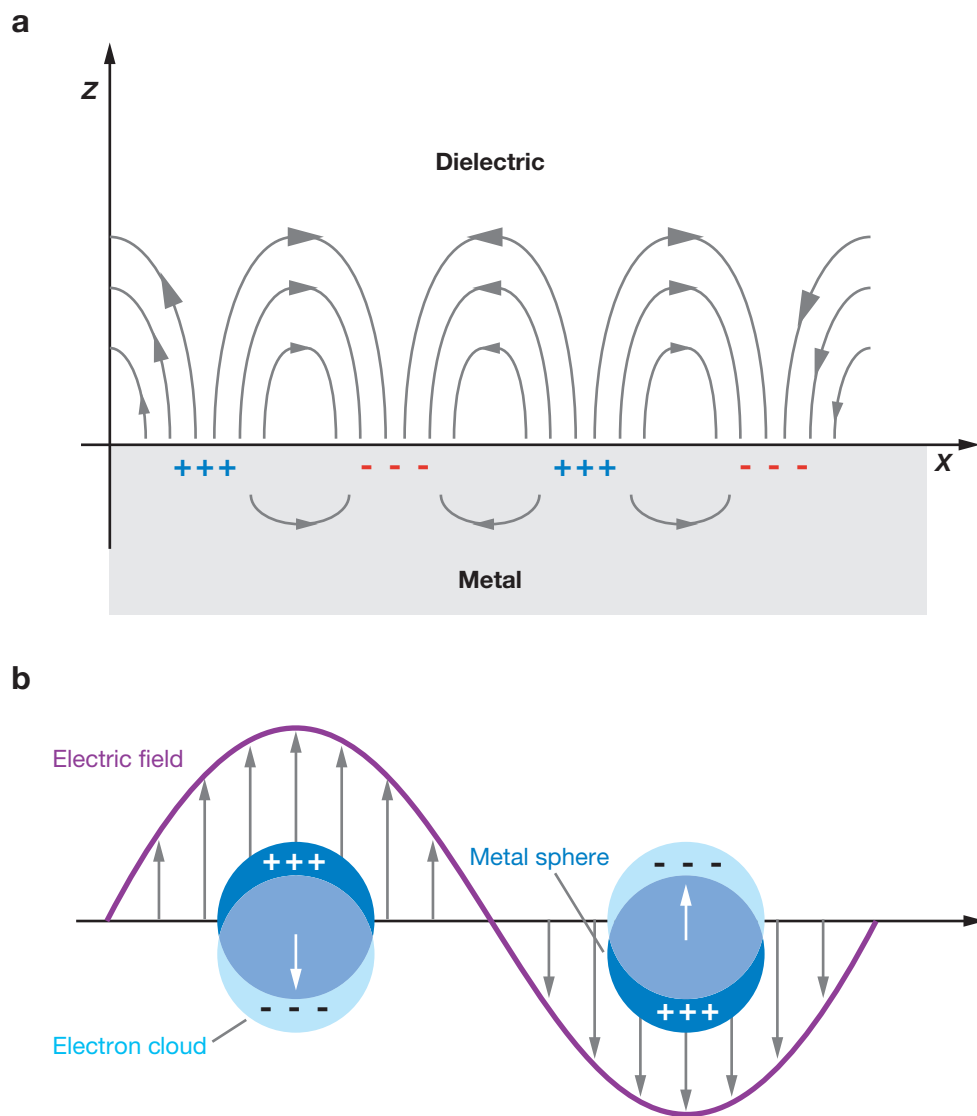
a

b

Figure 1

Schematic diagrams illustrating (*a*) a surface plasmon polariton (or propagating plasmon) and
(*b*) a localized surface plasmon.

provided a fundamental understanding of how plasmons are influenced by local struc-
ture and environment, they also suggested the usefulness of plasmons as a sensing
modality. Today, plasmon spectroscopy enjoys a reputation as an ultrasensitive method
for detecting molecules of both biological and chemical interest, in addition to its con-
tinued role in enabling surface-enhanced spectroscopic methods, including SERS,

surface-enhanced hyper-Raman scattering, surface-enhanced infrared spectroscopy, second harmonic generation, and surface-enhanced fluorescence (11, 12, 15, 16, 41, 60, 61).

Although SPR spectroscopy currently dominates commercial instrumentation, LSPR spectroscopy offers many of the same advantages for sensing and spectroscopy experiments, along with several additional benefits (21, 40). Both SPR and LSPR spectroscopy can provide thermodynamic and real-time kinetic data for binding processes. Moreover, although SPR spectroscopy provides much higher sensitivity to changes in the bulk refractive index than LSPR spectroscopy (25, 40), the response of the two techniques becomes comparable when measuring short-range changes in the refractive index owing to a molecular adsorption layer (40). This is a result of the much smaller sensing volume offered by LSPR sensors, as the EM-field-decay length is 40–50 times shorter than that of the SPR sensors (62, 63). Single-nanoparticle LSPR spectroscopy is another option, offering sensitivity that not only rivals, but can surpass, that of nanoparticle array-based LSPR spectroscopy (20, 33, 57, 64). Moreover, advances in both synthetic and lithographic fabrication techniques allow researchers to tune the LSPR wavelength throughout the visible, near-infrared, and into the infrared region of the EM spectrum, by varying the shape, size, and material of the nanoparticles that support the surface plasmons (57, 64–72). This offers additional flexibility when designing LSPR sensing experiments.

The remainder of this review on LSPR spectroscopy and sensing is organized as follows: First, we present several key equations for understanding the theory behind the LSPR. This is followed by a discussion of experimental techniques for fabricating metallic nanoparticles and performing spectroscopic measurements. Next, we present several fundamental studies of plasmon spectroscopy, illustrating key relationships that govern the LSPR spectral location and its sensitivity to the local dielectric environment. To round out our discussion, we provide specific examples of LSPR sensing experiments using both wavelength-shift and SERS spectroscopy.

THEORY

A full theoretical treatment of localized surface plasmons is quite lengthy and beyond the scope of this review. However, we refer the interested reader to the **Supplemental Appendix** for a complete derivation of several of these equations. (Follow the Supplemental Material link from the Annual Reviews home page at **http://www.annualreviews.org**.) For our more compact treatment, we consider a spherical nanoparticle of radius a that is irradiated by z-polarized light of wavelength λ (where a is much smaller than the wavelength of light λ; i.e., $a/\lambda < 0.1$). In this limit, the magnitude of the electric field appears static around the nanoparticle (as in **Figure 1b**), allowing us to solve Maxwell's equations using a quasi-static approximation (3, 43). The resulting solution for the EM field outside the particle is given by

$$E_{out}(x, y, z) = E_0\hat{\mathbf{z}} - \left[\frac{\varepsilon_{in} - \varepsilon_{out}}{(\varepsilon_{in} + 2\varepsilon_{out})}\right] a^3 E_0 \left[\frac{\hat{\mathbf{z}}}{r^3} - \frac{3z}{r^5}(x\hat{\mathbf{x}} + y\hat{\mathbf{y}} + z\hat{\mathbf{z}})\right]. \qquad (1)$$

Here, ε_{in} is the dielectric constant of the metal nanoparticle, and ε_{out} is the dielectric constant of the external environment. Because ε_{in} is strongly dependent on wavelength, the first term in square brackets determines the dielectric resonance condition for the particle. When the dielectric constant of the metal is roughly equal to $-2\varepsilon_{out}$, the EM field is enhanced relative to the incident field. In the case of silver and gold, this condition is met in the visible region of the spectrum, which has important implications for surface-enhanced spectroscopies. The size (a) and external dielectric constant (ε_{out}) also play key roles in determining the EM field outside the particle, consistent with experimental results.

Extinction spectrum: absorption plus elastic light-scattering spectrum

We calculate the extinction spectrum of the metal sphere as follows (73, 74):

$$E(\lambda) = \frac{24\pi^2 Na^3 \varepsilon_{out}^{3/2}}{\lambda \ln(10)} \left[\frac{\varepsilon_i(\lambda)}{(\varepsilon_r(\lambda) + \chi\varepsilon_{out})^2 + \varepsilon_i(\lambda)^2} \right]. \qquad (2)$$

Here, ε_r and ε_i are the real and imaginary components of the metal dielectric function, respectively. Again, we note the wavelength dependence of the metal dielectric function. Of additional interest is the factor of χ that appears in front of ε_{out}. The value of χ is 2 for the case of a sphere, but it takes on values as large as 20 to account for particle geometries with high aspect ratios (75). Because we can only solve the value of χ analytically for spheres and spheroids, and we must approximate it for all other geometries (43, 75), researchers have developed additional numerical methods; these include the discrete dipole approximation and the finite-difference time-domain methods (76–81). In these calculations, the particle of interest is represented as N finite polarizable elements, each of which can interact with the applied electric field. In the case of the discrete dipole approximation method, this interaction is modeled in the frequency domain, whereas the finite-difference time-domain method evaluates this interaction in the time domain. Both methods allow the evaluation of the extinction of particles of arbitrary shape and size, and the results typically match well with experimental results.

In addition to modeling the extinction of particles, several equations describe how the LSPR is used for both sensing and spectroscopic experiments. For example, the LSPR extinction (or scattering) wavelength maximum, λ_{max}, is sensitive to the dielectric constant ε (or refractive index, n; both are related by $\varepsilon = n^2$). Thus, changes in the local environment—such as through the presence of an adsorbed species—should cause a shift in λ_{max}. This leads to the following relationship (25, 82):

$$\Delta\lambda_{max} = m\Delta n \left[1 - \exp\left(\frac{-2d}{l_d} \right) \right]. \qquad (3)$$

Here m is the bulk refractive-index response of the nanoparticle(s); Δn is the change in refractive index induced by the adsorbate; d is the effective adsorbate layer thickness; and l_d is the characteristic EM-field-decay length (approximated as an exponential decay). This relationship is the basis of LSPR wavelength-shift sensing experiments, as illustrated in subsequent examples below.

We can describe the enhancement factor for SERS as shown (83, 84):

$$EF_{SERS}(\omega_v) = \frac{|E_{out}(\omega)^2| \, |E_{out}(\omega - \omega_v)^2|}{E_o^4} = \frac{\left[I_{SERS}(\omega_v) / N_{surf} \right]}{\left[I_{NRS}(\omega_v) / N_{vol} \right]}. \qquad (4)$$

This equation describes how the Raman enhancement effect is a result of enhancing both the incident excitation, $E_{out}(\omega)$, and the resulting Stokes' shifted Raman, $E_{out}(\omega - \omega_v)$, EM fields. The calculation of the enhancement factor from experimental measurements is given by the right-hand side of Equation 4—i.e., the SERS-enhanced Raman intensity, $I_{SERS}(\omega_v)$—normalized by the number of molecules bound to the enhancing metallic substrate, N_{surf}, divided by the normal Raman intensity, $I_{NRS}(\omega_v)$, normalized by the number of molecules in the excitation volume, N_{vol}. This equation is important for characterizing the enhancing ability of substrates of various material, geometry, and LSPR wavelength and is applied to several of the fundamental spectroscopy studies described below.

EXPERIMENTAL DETAILS

Nanofabrication

The ability to fabricate nanoparticles of varying shape, size, and material has been a major factor in advancing the understanding and application of LSPR spectroscopy. Whereas chemical synthetic techniques offer the ability to fabricate large quantities of nanoparticles (often with novel architectures and controlled crystallinity), lithographic techniques allow the fabrication of periodic arrays with specific particle shape, placement, and orientation. One particularly useful form of lithography is nanosphere lithography (NSL), which is a cost-effective and rapid means of producing several periodic array structures (56, 59, 85, 86). **Figure 2** illustrates the NSL process. Briefly, polymer nanospheres are drop coated on a substrate and allowed to self-assemble into a close-packed hexagonal array. This nanosphere mask allows the fabrication of several different LSPR substrates, all from the same masking procedure. In one case, metal is deposited (typically 15–100 nm) and then the nanosphere mask is washed away, leaving the triangular nanoparticle array shown in **Figure 2b** (56). In the second case, a thicker layer of metal (∼200 nm) is deposited over the nanospheres, producing a metal film over nanosphere (FON); this substrate is particularly effective for SERS applications owing to the stability of the local surface roughness on this curved substrate (**Figure 2c**) (41, 42, 87). A third approach is to use reactive-ion etching through the nanosphere mask to create small wells, into which metal can be deposited (88). In all cases, the resonance wavelength of the LSPR can be tuned simply by varying the diameter of the nanospheres in the mask, as well as the thickness of the deposited metal.

Electron-beam lithography, although more time-consuming and expensive, offers the advantage of creating nanoparticles of arbitrary size, shape, and spacing. Here, an electron beam is used to write a deposition mask directly into a polymer film; metal is then deposited through this mask and the film washed away, leaving behind the desired pattern. Researchers have used this technique to study plasmonic coupling between nanoparticles of arbitrary shape with different interparticle spacing (71, 89–91). Chemical syntheses provide another strategy for making particles of different shape and size, although one must realize and accommodate the effects of polydispersity (64–67, 69, 70, 92–95). By changing the reaction conditions and the
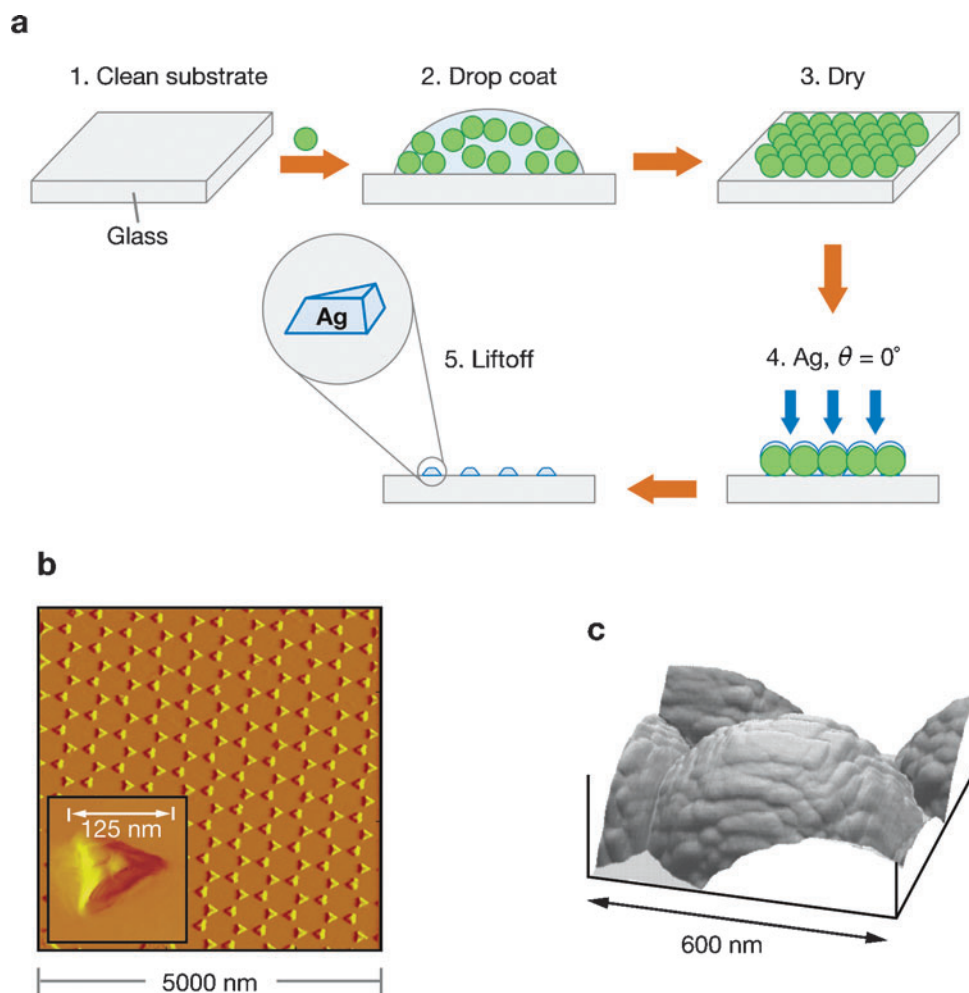
Figure 2

(*a*) Illustration of the process of nanosphere lithography (NSL) in which nanospheres are drop coated onto a surface and allowed to self-assemble into a hexagonally close-packed array (*steps 1–3*), followed by metal deposition (*step 4*), and (optional) removal of the nanosphere mask. (*b*) Atomic-force-microscope image of an NSL-fabricated nanoparticle array in which the nanosphere mask has been removed. (*c*) Atomic-force-microscope image of a film-over-nanosphere (FON) substrate in which the nanospheres remain on the surface.

stabilizing surfactant, researchers have produced a wide variety of shapes, including triangles, cubes, prisms, tetrahedra, bipyramids, and even stars (57, 64, 66, 67, 92, 93). As an interesting aside, the NSL-produced nanoparticles described above can also be released into solution via simple chemical functionalization; this provides an alternate approach for making particles in solution without the need for any synthetic chemistry (96).

Spectroscopic Measurements

Figure 3 shows several approaches to the measurement of nanoparticle LSPR spectra. The most straightforward is transmission ultraviolet-visible spectroscopy (**Figure 3a**). Here one measures the extinction spectrum (absorption plus scattering) of the nanoparticles by recording the wavelength dependence of the light passing through the sample. In the case of nontransparent samples (such as the FONs described above), one must use a reflective geometry (**Figure 3b**) (42). Here, a fiber bundle is used both to direct the excitation light to the sample (center fiber), as well
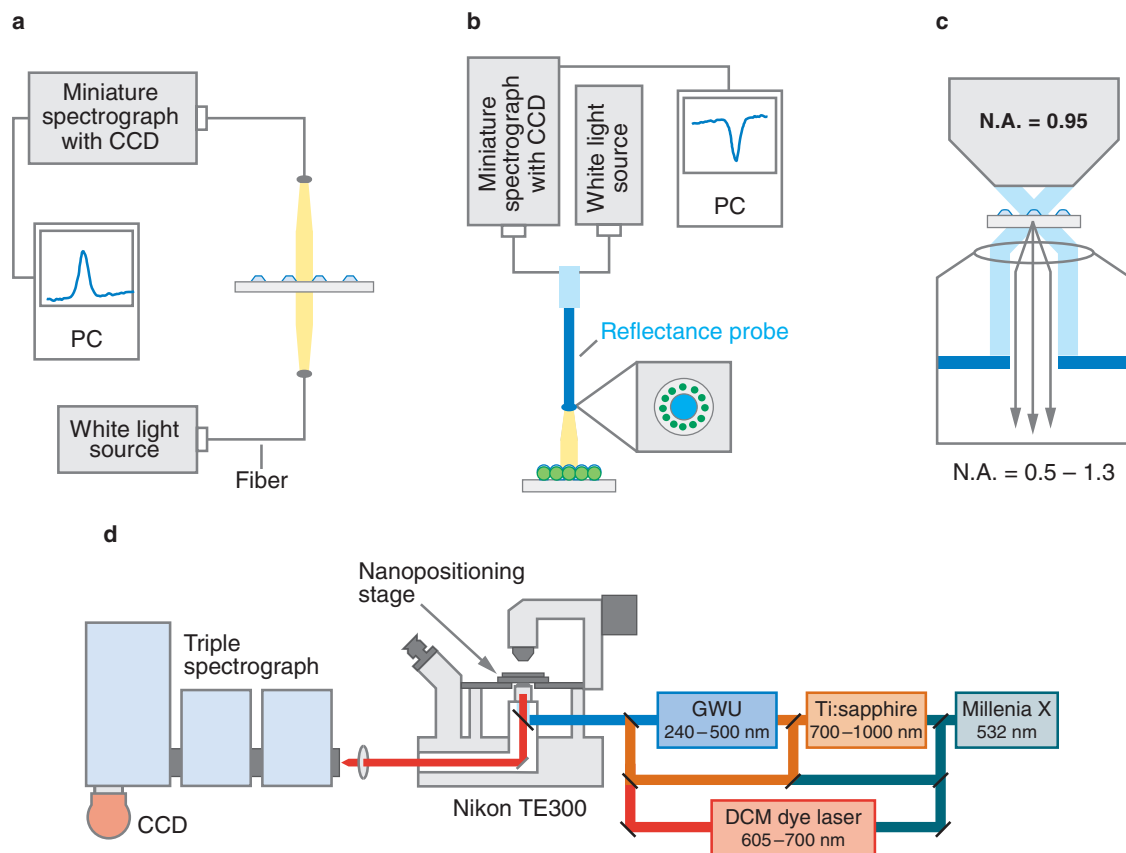
Figure 3

(*a*) Transmission and (*b*) reflectance geometries for measuring extinction spectra of nanoparticle arrays. (*c*) Dark-field scattering experimental setup using a high-numerical aperture dark-field condenser and a low-numerical aperture microscope objective for measuring single-nanoparticle scattering spectra. (*d*) Experimental setup for measuring surface-enhanced Raman scattering in an epi-illumination geometry using a wavelength-scanned laser-excitation system and a triple spectrograph coupled with a charge-coupled device (CCD) camera. Reproduced with permission from Reference 84. Copyright 2005 American Chemical Society.

as to collect the light reflected from the surface (radial array of fibers). Whereas the transmission geometry yields the LSPR wavelength as a maximum value in the extinction curve, the reflected geometry yields the LSPR wavelength as a minimum value (because light absorbed or scattered by the sample is not reflected back).

For samples in which small regions or even single nanoparticles are interrogated, dark-field light-scattering measurements are extremely powerful. In this case, white light is introduced to the sample at a high angle, and scattered light is collected at a lower angle. **Figure 3c** shows an example of this in which a high-numerical aperture condenser brings light to the sample, and a low-numerical aperture microscope objective collects the scattered light at low angles. This can also be accomplished using a dark-field microscope objective, which serves the dual function of bringing the high-angle excitation light to the sample, as well as collecting the low-angle scattered light (much like the fiber used in the reflectance geometry above). In both cases, the scattered light is then directed to a spectrometer and detector, such as a charge-coupled device camera, yielding an LSPR spectrum of the sample.

For SERS measurements, the sample is excited by a laser (optimally to the blue of the LSPR of the metal substrate), and the Raman scattered light is passed through a spectrometer and onto a detector. The excitation light is typically directed to the sample at either a glancing angle or by using a microscope objective in epi-illumination. **Figure 3d** shows the latter configuration; this experimental setup was used for the wavelength-scanned SERS excitation–spectroscopy experiments described in the following section.

SPECTROSCOPY

Fundamental spectroscopic studies on plasmonic materials provide an understanding of the properties that govern both the LSPR wavelength and the surface enhancement factor of these substrates, which is critical when designing materials for sensing applications. In this section, we describe experiments that demonstrate several of these fundamental relationships and explain how these can impact—and hopefully improve—LSPR sensing experiments.

Localized Surface Plasmon Resonance Size and Shape Dependence

Because the shape and size of a metallic nanoparticle dictate the spectral signature of its plasmon resonance, the ability to change these two parameters and study the effect on the LSPR is an important experimental challenge. Researchers first systematically studied this using NSL-fabricated arrays with variable diameter nanosphere masks as well as different Ag film thicknesses (97). A second approach is to use electrochemistry to oxidize the nanoparticles, thus modifying their surface structure in a highly controlled manner (68). For these experiments, NSL-fabricated silver triangles were prepared on an indium tin oxide substrate and subjected to multiple chronocoulometric runs. **Figure 4** shows the results of these experiments. The particular power of this approach is that the triangles are selectively oxidized (first at the bottom edges, then at the triangular tips, and finally from the top face), allowing the LSPR response

Chronocoulometry: electrochemical measurement of charge versus time following a step-wise change in the applied potential
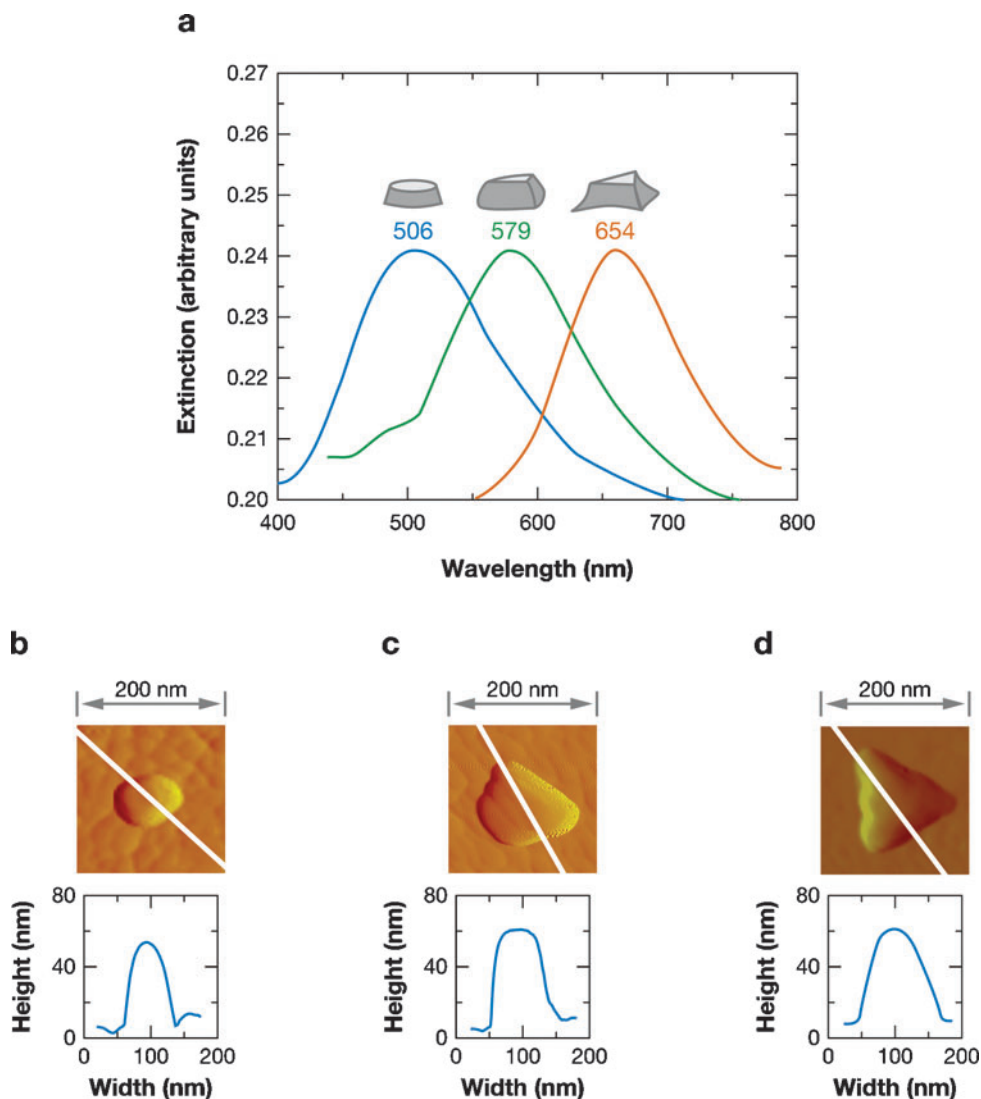
Figure 4

Localized surface plasmon resonance (LSPR) spectra and atomic-force-microscope images of
Ag nanoparticles on indium tin oxide. (*a*) The LSPR λ_{max} of the Ag nanoparticles shifts
toward shorter wavelengths after subsequent chronocoulometry measurements.
(*b*) Atomic-force-microscope image following two chronocoulometry runs, (*c*) following one
chronocoulometry run, and (*d*) before any electrochemical oxidation. Prior to electrochemical
oxidation, the NSL-fabricated nanoparticles have their characteristic triangular shape (*b*) and
the LSPR spectrum shown in orange (*a*); however, after each chronocoulometric run, the
triangular tips are rounded (*b,c*) and the LSPR spectrum shifts to higher energy (*a, green and
blue curves*). The cross section of each atomic-force-microscope image illustrates the changing
in-plane width of the nanoparticles following oxidation. Reproduced with permission from
Reference 68. Copyright 2005 American Chemical Society.

to morphological changes to be directly correlated. For example, we can study the relation between the in-plane width and the LSPR because the triangle height does not change during the initial oxidation events. Thus, electrochemical oxidation is a unique tool for changing the shape and size of NSL-fabricated nanoparticles in a controlled manner, allowing the observation of systematic trends.

A third approach for examining the relationship between shape, size, and the LSPR wavelength is through single-nanoparticle spectroscopy (20, 33, 57, 58, 98, 99). Because there is inherent heterogeneity among individual nanoparticles, each LSPR spectrum is different, revealing the true distribution of resonance wavelengths (20, 98). For example, silver colloids prepared via a citrate reduction have a variety of shapes and sizes, which results in a vast array of LSPR spectra (20, 99). The different shapes show different refractive-index sensitivities, with rods showing the highest sensitivity followed by triangles, then spheres (20). More refined synthetic approaches produce nanoparticles with less heterogeneity in shape and size and even higher refractive-index sensitivity (57, 69, 70). For example, triangular nanoprisms functionalized with alkanethiols of increasing chain length show a 4.4-nm shift in maximum LSPR wavelength per each additional methyl group, the highest short-range, single-particle refractive-index sensitivity reported thus far (100). Moreover, the height, width, and tip sharpness of these nanoprisms can be controlled, allowing the characterization of the relationships between these structural properties and both the LSPR wavelength and refractive-index sensitivity (69, 100).

Single-particle spectroscopy has also revealed unique spectroscopic properties. For example, when individual cubic nanoparticles with a 30-nm edge length are placed on a dielectric substrate, the LSPR spectrum reveals two peaks: a broad red peak that is also present in solution, and a narrow blue peak that emerges owing to its interaction with the dielectric substrate (57). For a nanoparticle to yield a new plasmon resonance peak when placed on a dielectric surface, it must satisfy two conditions: (*a*) Its near fields must be most intense at the polar (rather than the equatorial) regions of the nanoparticle, and (*b*) it must be thicker than the skin depth of the material (~25 nm for silver). This new peak also shows improved refractive-index sensitivity owing to its narrow line width, defined by a figure of merit in which the bulk refractive-index sensitivity is divided by the full width half max of the peak (57). Thus, this novel cubic architecture may be valuable for future LSPR sensing experiments.

Localized Surface Plasmon Resonance Distance Dependence

Equation 3 models the change in the LSPR wavelength as the refractive index of the nanoparticles' surroundings is changed. In this equation, the EM-field decay length was approximated as a single exponential decay with characteristic decay length l_d. Although Equation 3 provides a reasonable approximation of the behavior of the field, it provides no insight into the effect of nanoparticle structure on the EM-field decay length and related properties. To understand this relationship, researchers have conducted initial experiments by measuring the LSPR wavelength shift of NSL-fabricated triangles using self-assembled alkanethiol mono- and multilayers to probe the short-range and long-range distance dependence of the field, respectively (63,

101). The results of the short-range studies suggest that the LSPR shift decreases when either (*a*) the nanoparticle in-plane width increases or (*b*) the nanoparticle out-of-plane height increases, whereas the long-range studies suggest the opposite trend (63, 101). However, these experiments had less-than-optimal control over layer thickness and local refractive index owing to the effects of alkanethiol-chain tilt angle and packing density.

Recently, researchers carried out a second-generation LSPR distance-dependence study. They employed atomic layer deposition (ALD) to provide the ultimate in distance resolution and a highly uniform refractive index independent of layer thickness (102–104). Here, a single atomic layer of alumina (Al_2O_3) is deposited onto the nanoparticle surface, which provides 1.1-Å distance resolution (104). **Figure 5*a*** shows the LSPR shift from NSL-fabricated nanoparticles of varying out-of-plane heights as the alumina film thickness increases (62). The nanoparticles show LSPR shifts even with a single atomic layer of Al_2O_3, demonstrating the impressive sensitivity of nanoparticles to their local environment. However, this sensitivity diminishes as the nanoparticle out-of-plane height increases: The thickest nanoparticles show
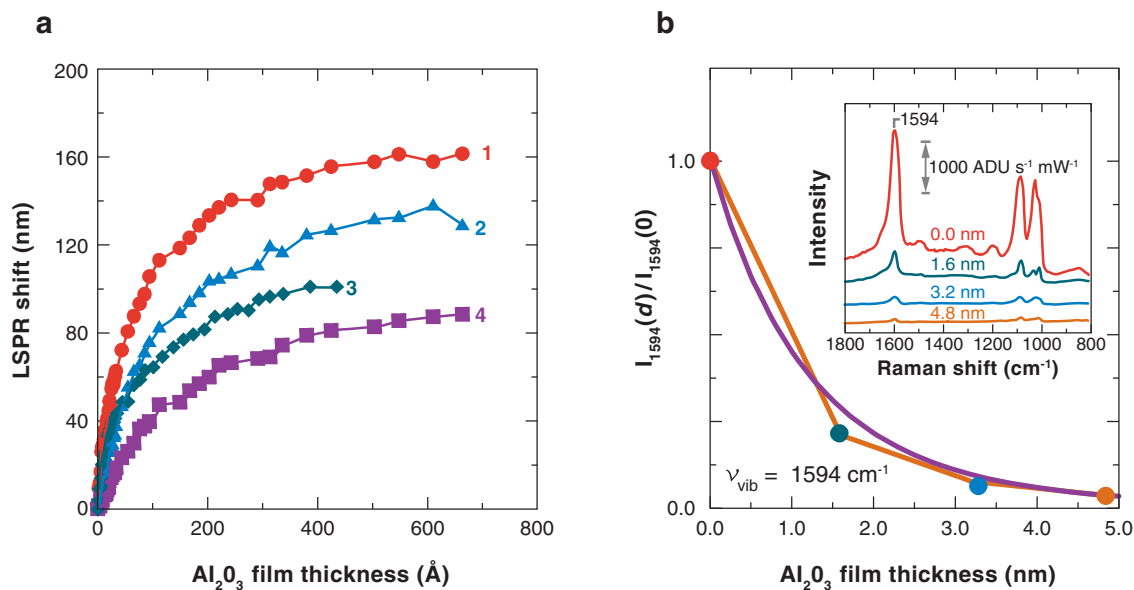
Atomic layer deposition (ALD): a self-limiting growth process that produces a single monolayer of material per deposition cycle

Figure 5

(*a*) Localized surface plasmon resonance (LSPR) shift versus Al_2O_3 film thickness for particles of different shape and size. Data are presented for silver triangular nanoparticles with in-plane widths of 90 nm and thicknesses of (*1*) 30 nm, (*2*) 40 nm, and (*4*) 51 nm, as well as Ag hemispherical nanoparticles with an in-plane width 104 nm and thickness of 52 nm (*3*). Reproduced with permission from Reference 62. Copyright 2005 American Chemical Society. (*b*) Plot of normalized surface-enhanced Raman scattering (SERS) intensity as a function of alumina thickness for the 1594 cm^{-1} band of pyridine. (*Inset*) SERS spectra from which the normalized SERS intensity is calculated. From Reference 105; reproduced with permission of The Royal Society of Chemistry.

less of an LSPR shift in response to the alumina layer than the thinnest nanoparticles (**Figure 5a**, curves 4 and 1, respectively). Moreover, the LSPR shift begins to flatten out (at a layer thickness of approximately 600 Å), owing to the decay of the EM field further from the particle surface.

Because the enhanced EM field decreases further from the nanoparticle surface, ALD also offers a mechanism for probing the distance dependence of SERS (105). **Figure 5b** shows the SERS spectrum of pyridine spaced from the nanoparticle surface by alumina layers of variable thickness. The spectrum is most enhanced when the particle is directly adsorbed to the metal surface (an alumina layer thickness equal to 0 nm). As the thickness of the alumina spacer increases, the intensity of the SERS spectrum decreases. These data can be fit to Equation 5 as shown (105, 106):

$$I = \left(1 + \frac{r}{a}\right)^{-10}, \tag{5}$$

where I is the intensity of the Raman mode, a is the size of the enhancing nanoparticle feature, and r is the distance from the surface to the adsorbate. The best fit line to Equation 5 is shown in **Figure 5b** (curve 4) and yields a value of $a = 12.0$ nm. Moreover, the distance at which the SERS intensity decreases by a factor of 10 is 2.8 nm for this particular sample, showing that SERS is a long-range effect. Thus, it is now possible to probe the SERS enhancement as a function of distance and nanoparticle geometry with angstrom resolution, experiments that are currently in progress.

Plasmon- and Wavelength-Scanned Surface-Enhanced Raman Scattering

Although it was well-known that the LSPR of the metallic substrate should be close to the excitation wavelength used for SERS, a systematic study of the relationship between the two had not been completed. However, recent work that measured the Raman enhancement factor as a function of either the LSPR or the excitation wavelength has developed this relationship more clearly (84, 107). In the initial studies, researchers measured the SERS enhancement factor as a function of the LSPR spectral position at a constant laser-excitation wavelength (107). **Figure 6a** shows the Raman enhancement factor of the 1081 cm^{-1} peak from benzenethiol adsorbed to NSL-fabricated arrays with different LSPR wavelengths. The figure illustrates that the maximum enhancement occurs when the plasmon resonance is to the red of the fixed excitation wavelength ($\lambda_{exc} = 632.8$ nm) and to the blue of the Stokes-shifted Raman band (shifted 1081 cm^{-1} from λ_{exc}). Additional experiments of this type demonstrate that the largest SERS enhancement factor is observed when the LSPR falls within a 120-nm window that includes both the excitation wavelength and the Raman-shifted wavelength.

An alternative and more general approach is to use a single NSL-fabricated nanoparticle array sample with a constant LSPR wavelength and scan the excitation wavelength using a tunable laser system (**Figure 3d**). **Figure 6b** shows data from such an experiment in which the enhancement factor of the same 1081 cm^{-1} peak
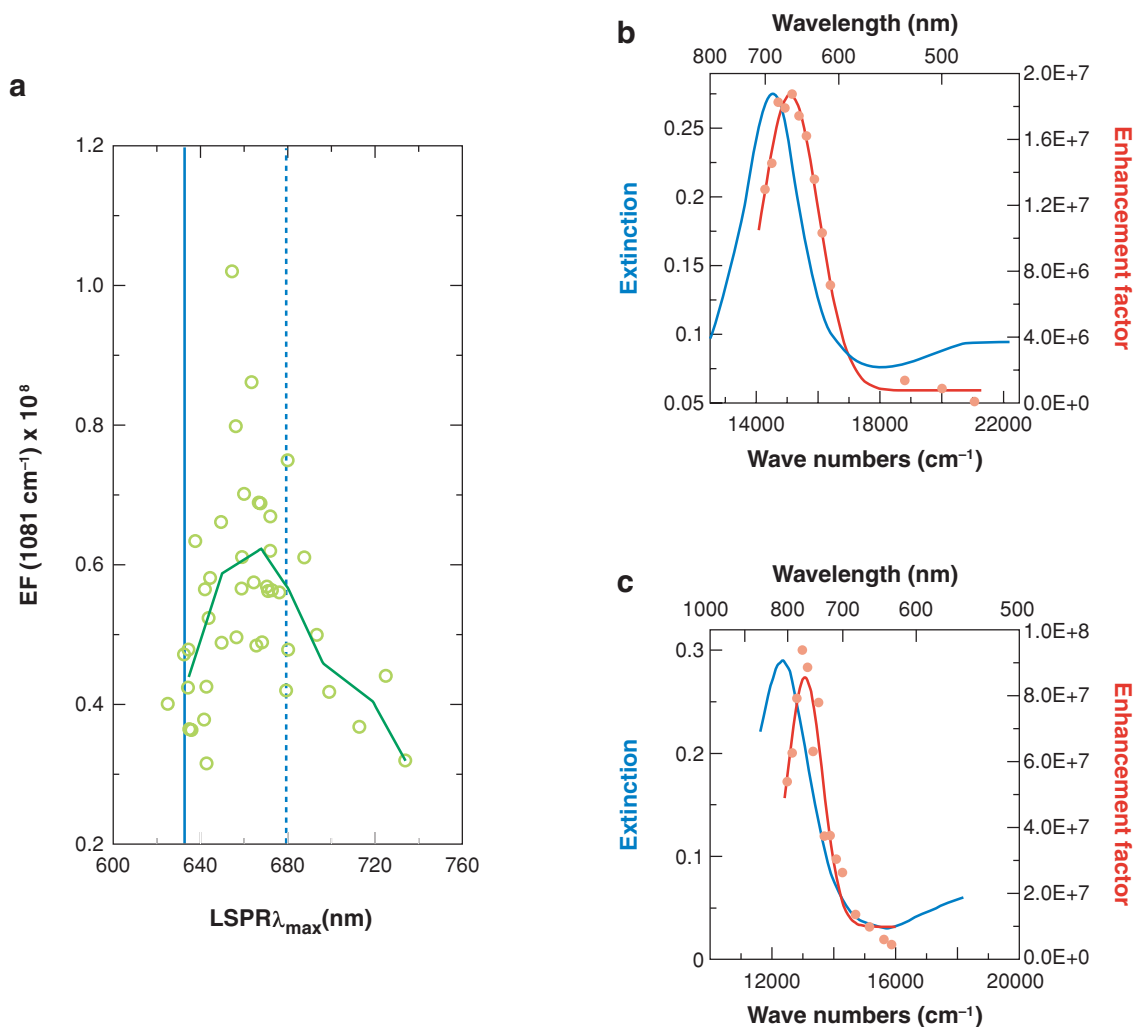
Figure 6

(*a*) Plasmon-sampled surface-enhanced Raman excitation spectrum of the 1081 cm^{-1} peak of benzenethiol (*dashed line*) excited at 632.8 nm (*solid line*). The enhancement factor is highest when the plasmon wavelength is between the Raman excitation and emission energies. Reproduced with permission from Reference 107. Copyright 2003 American Chemical Society. (*b*) Wavelength-scanned surface-enhanced Raman excitation spectra of the 1081 cm^{-1} peak of benzenethiol, LSPR λ_{max} = 690 nm, profile fit maximum at 662 nm. (*c*) Wavelength-scanned surface-enhanced Raman excitation spectra of the 1575 cm^{-1} peak of benzenethiol, LSPR λ_{max} = 810 nm, profile fit maximum at 765 nm. Reproduced with permission from Reference 84. Copyright 2005 American Chemical Society.

from benzenethiol is monitored as the excitation wavelength varied between 475 and 800 nm. The excitation spectrum shows the highest SERS enhancement factor when the excitation wavelength is to the blue of the LSPR wavelength, consistent with the plasmon-scanned results above. (The axes on this plot are in units of increasing wave number and thus decreasing wavelength.) Based on Gaussian fits to the spectra, the shift between the maximum energy of the excitation profile and the LSPR spectrum is 613 cm^{-1}, placing it roughly at the midpoint of the shift between the excitation and the Stokes Raman scattering energies (i.e., 1081 cm^{-1}). The 1575 cm^{-1} peak of benzenethiol shown in **Figure 6c** also demonstrates this relationship. Again, the shift between the excitation wavelength producing the maximum enhancement and the peak in the extinction spectrum is 726 cm^{-1}, or roughly half of the shift between the excitation and Raman-shifted scatter.

By repeating this measurement on different vibrational bands, we see a distinct trend emerge: For higher-energy Raman transitions, the shift between the excitation profile and the LSPR spectrum also moves to higher energy. This is because the LSPR should be located at some intermediate energy between the excitation and Raman EM fields to provide the maximum enhancement of the two. As the Raman transition moves to higher energy, the gap between the excitation and Raman energies widens, and the LSPR maximum must shift to remain roughly midway between the two. In this case, the LSPR is static, so the effect is reversed: The excitation profile shifts to higher energy. This is in agreement with the EM-enhancement mechanism and is an important outcome of these wavelength-scanned SERS experiments. Moreover, these experiments illustrate the importance of optimizing the plasmon and excitation wavelengths to achieve maximum SERS enhancements; enhancements of nearly 10^8 can be produced when experimental conditions are properly optimized (**Figure 6c**). Although ensemble-averaged SERS enhancement factors of 10^8 are the highest we have measured to date, there is good reason to believe that future experiments will reveal substantially higher values for systems involving highly crystalline single nanoparticles and specific, finite nanoparticle assemblies (108).

Molecular resonances: electronic (or vibrational) resonances in molecules that absorb photons in the same energy region as the localized surface plasmon resonance

Localized Surface Plasmon Resonance Spectroscopy Near Molecular Resonances

Surface-enhanced resonance Raman scattering (SERRS) has been known for producing enhancement factors of the order 10^{11}–10^{12} dating back to the original report of SERS (1, 107). In SERRS, the Raman excitation light is of sufficient energy to promote an electronic transition in the molecule of interest, from the ground to some electronically excited state. When the LSPR of the enhancing substrate is also in the proper energy region, this provides SERRS enhancement factors that are roughly the product of the enhancement factors for nonresonant SERS of the substrate and the resonance Raman spectrum of the adsorbate (107). However, there had previously not been any study on the effect of an electronically resonant molecule on the spectral position and lineshape of the nanoparticle plasmon resonance.

To study this relationship, recent work focused on the LSPR shift induced by the adsorption of a molecule whose absorption spectrum is in the same energy region as

the plasmon resonance (109). [2, 3, 7, 8, 12, 13, 17, 18-Octakis(propyl) porphyrazi-nato] magnesium (II) has the solution-phase absorption curve shown in **Figure 7a**. When this molecule is adsorbed on NSL-fabricated nanoparticles with LSPR wavelengths both near and far from the molecular resonance, the shift is quite different (**Figure 7a**) (109). When the LSPR λ_{max} is close to the molecular resonance, the shift is either enhanced (**Figure 7b**) or suppressed (**Figure 7d**). In contrast, when the LSPR λ_{max} is far from the molecular resonance, the shift is less dramatic and closer to expectations based on a simple refractive-index change (**Figure 7c**). This result suggests that it may be possible to optimize the LSPR shift response for sensing experiments in which the analyte of interest has an electronic resonance in the visible or infrared region of the spectrum (see below).

LOCALIZED SURFACE PLASMON RESONANCE SENSING

Whereas the above section describes several fundamental spectroscopic relationships and their impact on LSPR sensing, this section focuses on sensing molecules of biological and chemical interest. We focus on two different sensing modes—wavelength-shift LSPR sensing and SERS—and their application to several different systems.

Localized Surface Plasmon Resonance Wavelength-Shift Sensing

The most common method for LSPR sensing is the wavelength-shift measurement, in which the change in the maximum (or minimum) of the LSPR extinction curve is monitored as a function of changes in the local dielectric environment caused by analyte adsorption. This relationship is described in Equation 3, and has been demonstrated for a number of systems in which either the bulk-solvent refractive index or the length of a molecular adsorbate (i.e., a linear alkane chain) is changed (20, 24, 32, 46, 57, 88, 98). Coupling two plasmonic nanoparticles also leads to a shift in λ_{max}. Researchers have demonstrated this for the released NSL-fabricated triangles described above, which were coupled using alkanedithiols (96), and more recently, for Au spheres linked by double-stranded DNA of varying length (110, 111).

This sensitivity to local environment can be expanded to sensing biological molecules such as proteins and antibodies. Initial demonstrations of this principle measured the shift in λ_{max} on binding of either streptavidin or antibiotin to biotin-functionalized nanoparticle arrays (82, 112). Experiments measuring the binding of concanavalin A to mannose-functionalized nanoparticles followed these first demonstrations (21). **Figure 8a** shows the real-time kinetic response of the LSPR shift for mannose-functionalized nanoparticles of different thickness on exposure to concanavalin A followed by washing with buffer. In all cases, the LSPR λ_{max} changes in response to the concanavalin A with a similar time constant but with a different overall shift magnitude. This agrees with the distance-dependence experiments because the LSPR wavelength-shift response was largest for the thinnest nanoparticles. These experiments demonstrate the importance of the fundamental spectroscopic studies described above for guiding the design of LSPR sensing experiments.
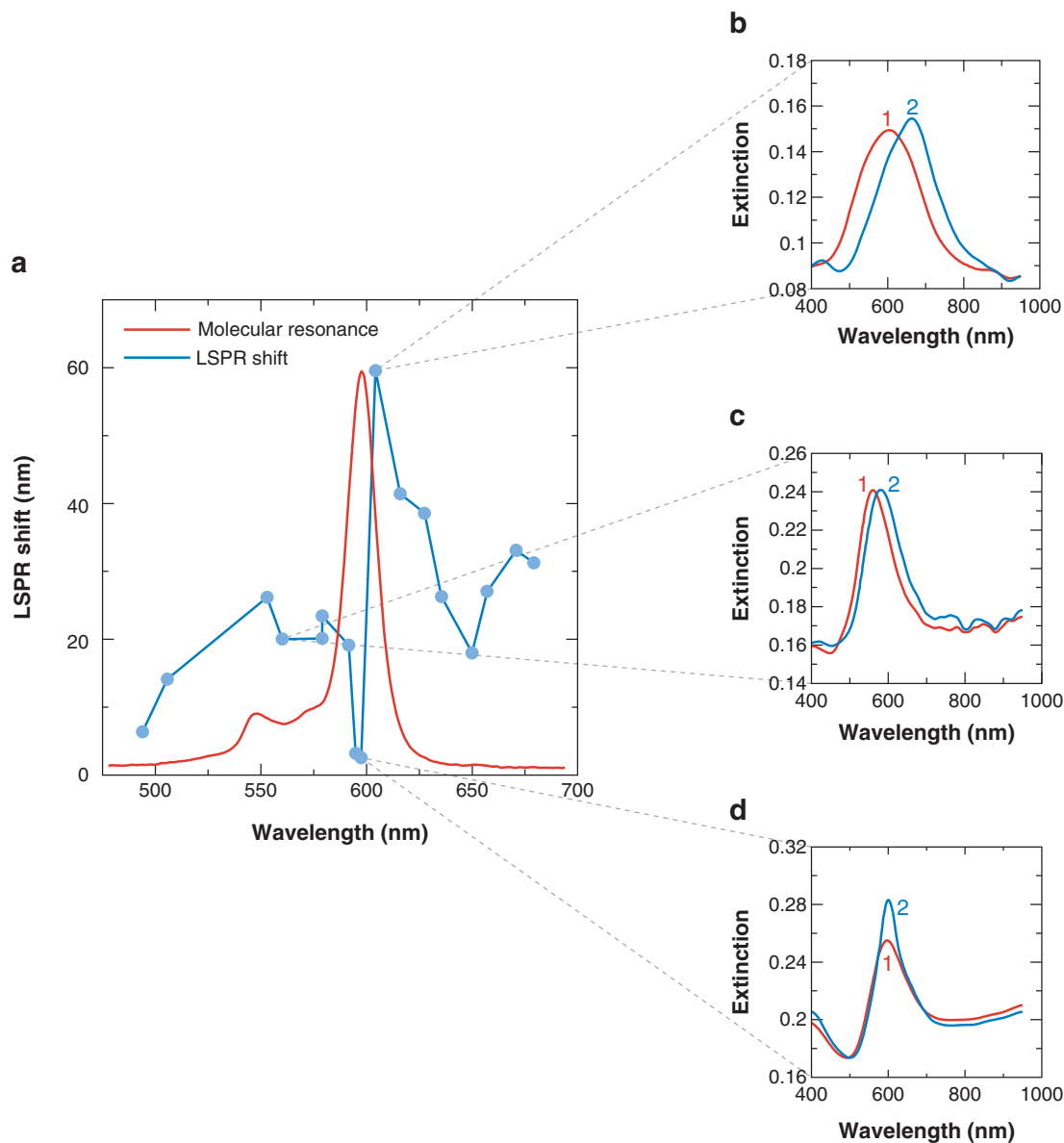
Figure 7

(*a*) Localized surface plasmon resonance (LSPR) shift induced by [2, 3, 7, 8, 12, 13, 17, 18-Octakis(propyl) porphyrazinato] magnesium (II) (MgPz) adsorption to Ag nanoparticles versus initial nanoparticle LSPR wavelength (*blue dots*). The absorption spectrum of the MgPz is also shown (*red line*). (*b–d*) LSPR spectra before and after MgPz adsorption both (*b, d*) near and (*c*) far from the molecular resonance. Measured LSPR shifts are (*b*) 59.6 nm, (*c*) 20.0 nm, and (*d*) 2.5 nm. Reproduced with permission from Reference 109. Copyright 2006 American Chemical Society.
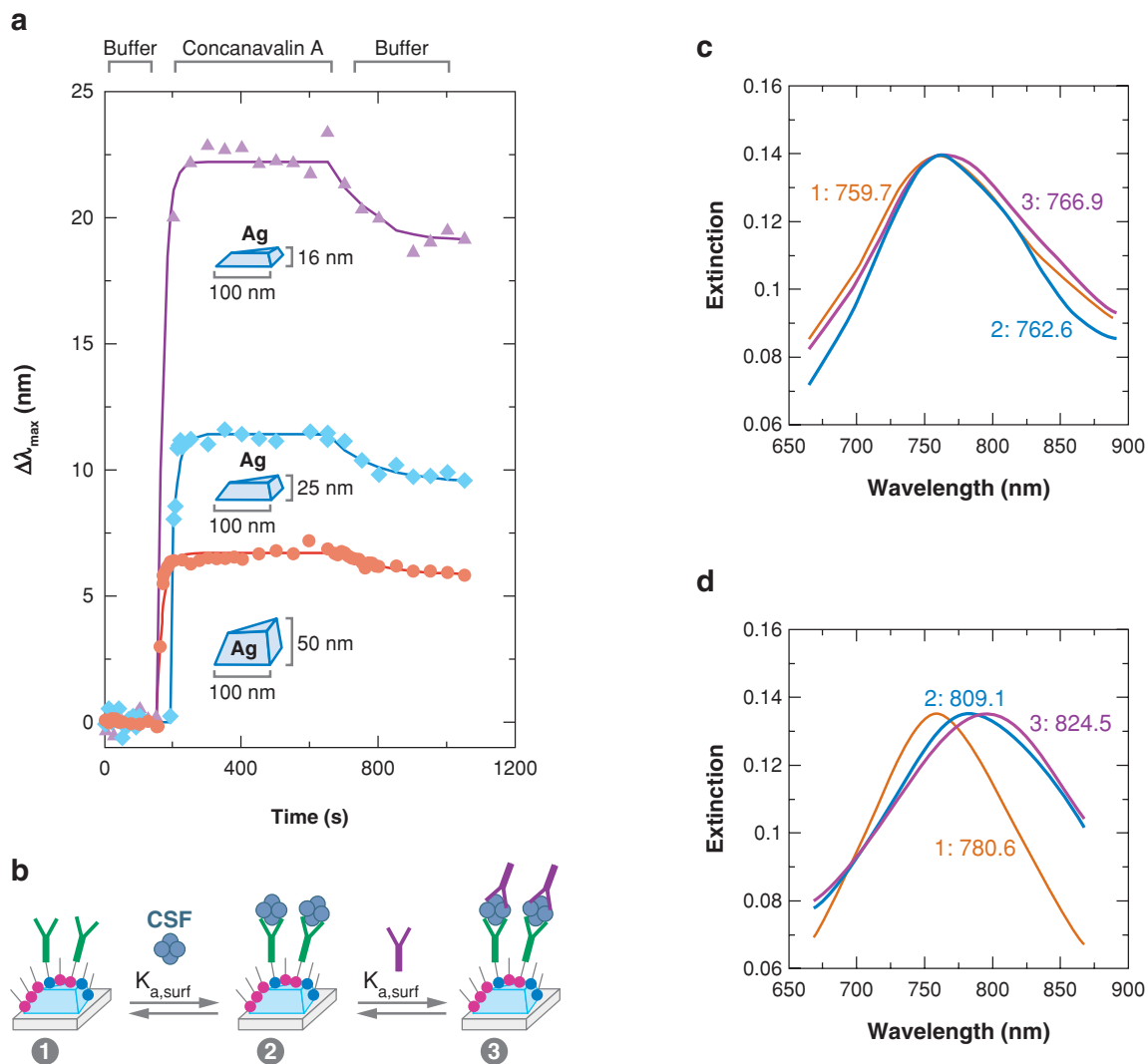
Figure 8

(*a*) Real-time response of mannose-functionalized Ag nanosensor of different out-of-plane heights as 19-μM concanavalin A is injected in the cell following buffer injection. The solid lines are provided as guides. Reproduced with permission from Reference 21. Copyright 2004 American Chemical Society. (*b*) Surface chemistry for the possible amyloid-beta-derived diffusible ligand (ADDL) detection in human cerebrospinal fluid (CSF) samples using the antibody sandwich assay. The three steps include (*1*) functionalization with 100-mM anti-ADDL, (*2*) the introduction of human CSF, and (*3*) the introduction of the second capping antibody. (*c*) Localized surface plasmon resonance spectra for each step of the assay for an age-matched control patient. (*d*) LSPR spectra for each step of the assay for an Alzheimer's patient. Reproduced with permission from Reference 17. Copyright 2005 American Chemical Society.

Perhaps the most biomedically relevant demonstration of LSPR sensing has been the work in which a biomarker for Alzheimer's disease, amyloid-beta-derived diffusible ligand (ADDL) (113–115), has been sensed using LSPR spectroscopy (17, 18). For these experiments, researchers developed a sandwich-format assay (**Figure 8***b*): First the nanoparticle array is functionalized with an antibody for the ADDL molecules; then the ADDLs are allowed to bind to the antibodies; and finally, a second capping antibody is introduced that can bind to the surface-bound ADDL and complete the sandwich assay. Initial experiments using synthetic ADDLs showed that ADDL concentrations on the order of 100 fM could be detected (17). Next, the experiments were repeated using cerebrospinal fluid (CSF) from both an Alzheimer's patient, as well as an age-matched control (17). The results from these experiments are shown in **Figures 8***d,c*, respectively. In **Figure 8***c*, the CSF from an age-matched control patient is exposed to the anti-ADDL functionalized nanoparticles; the shift in the LSPR spectrum is modest after both initial CSF exposure as well as the introduction of the second capping antibody ($\Delta\lambda_{max} = 2.9$ and 4.3 nm, respectively). **Figure 8***d* shows the data from an Alzheimer's patient. Here, the binding of the ADDLs in the CSF induces a shift of 28.5 nm, with a further shift of 15.4 nm after the second antibody is introduced. The researchers obtained a similar result when they used brain extract instead of CSF. Thus, LSPR spectroscopy is a promising technology for sensing this biomarker of Alzheimer's disease in a clinical setting. Moreover, this approach can be broadly generalized, allowing the diagnosis of any disease with an associated biomarker and antibody pair (such as ovarian cancer) (116).

Sensing experiments can also benefit from the introduction of an electronically resonant analyte (as described above). This has been demonstrated recently using cytochrome P450, which changes its absorption spectrum on the binding of small molecules such as camphor (117). As with previous examples above, the adsorption of the cytochrome P450 to the nanoparticle surface leads to a red shift in the LSPR wavelength owing to the change in the local refractive index. However, the binding of camphor to the adsorbed cytochrome P450 leads to a blue shift in the absorption spectrum of the protein, which, in turn, induces a corresponding blue shift in the LSPR spectrum (117). Thus, small-molecule binding, which normally does not yield a large-enough refractive-index change to induce a detectable LSPR shift, can now be sensed using LSPR spectroscopy near an electronic resonance.

Surface-Enhanced Raman Scattering Sensing

A second application in which the LSPR plays an important role is SERS-based sensing. As described above, it is important for the LSPR of the enhancing substrate to be properly matched with the Raman excitation and scattering wavelengths (84, 107). Here we describe several examples in which SERS is used for biological sensing experiments.

Recent work has focused on the detection of an anthrax biomarker, calcium dipicolinate (CaDPA), using SERS on both bare and alumina-modified silver FON substrates (**Figure 9***a*) (42, 118). *Bacillus subtilis* spores (a harmless simulant of *B. anthracis*) are sonicated in dilute nitric acid to extract the CaDPA; this solution is then deposited

ADDL:
amyloid-beta-derived diffusible ligand
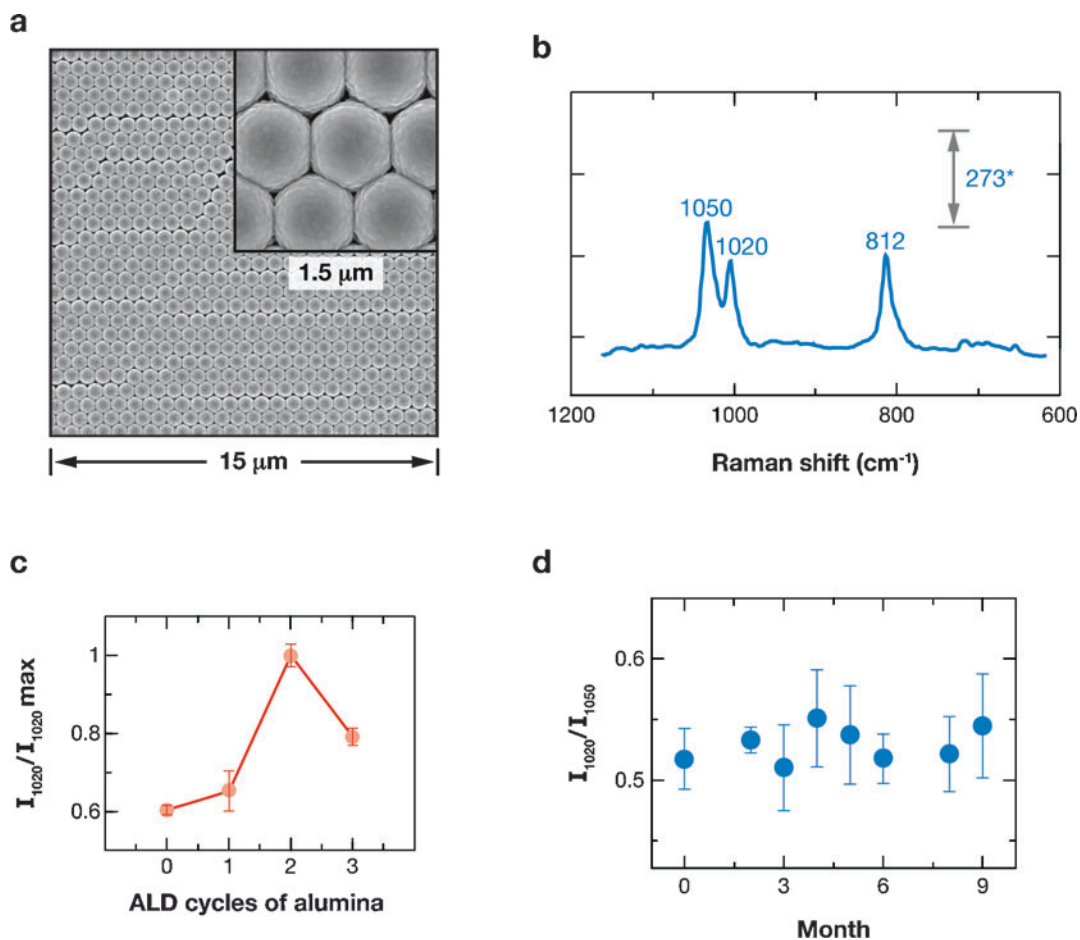
CaDPA: calcium dipicolinate

Figure 9

(*a*) Scanning-electron-microscope images of alumina-modified Ag film over nanosphere
(FON) substrates. (*b*) Surface-enhanced Raman scattering (SERS) spectrum of 2×10^{-5} M
CaDPA in 0.2 μL, 0.02 M HNO_3 on alumina-modified silver FON substrate. *273 = adu s^{-1}
mW^{-1}; adu, analog to digital converter units on th**e** CCD detector; s, seconds of data
collection time; mW, millwatts of laser power. (*c*) The alumina thickness effect on the SERS
intensity. The spectral intensities at 1020 cm^{-1} are plotted versus atomic layer deposition
(ALD) cycles and normalized against the highest measured intensity, in this case after two
ALD cycles. (*d*) The intensity ratio (I_{1020}/I_{1050}) variation with time for an alumina-modified
silver FON (two ALD cycles) over a nine-month period. Reproduced with permission from
Reference 118. Copyright 2006 American Chemical Society.

onto a silver FON (both bare and alumina modified); and the SERS spectrum is mea-
sured as shown in **Figure 9*b***. The peak at 1020 cm^{-1} is indicative of the CaDPA,
whereas the 1050 cm^{-1} peak owing to nitric acid provides an internal standard. In
Figure 9*c*, the intensity of the 1020 cm^{-1} peak is plotted with an increasing number
of alumina monolayers. **Figure 9*c*** shows two competing effects: Initially the intensity

of the 1020 cm^{-1} peak increases because alumina is acting as a capture layer for the analyte (118). However, after three cycles of alumina deposition, the Raman signal decreases owing to the drop-off in EM-field enhancement, in analogy to the distance-dependence study shown in **Figure 5b**. Using this scheme, the detection limit is 1400 spores, better than the previously reported limit of 2600 spores for bare silver surfaces and well below the infectious dose of 10^4 spores (42). Moreover, the alumina layer protects the FON surface from oxidation, improving the temporal stability of these SERS substrates to greater than 270 days after fabrication (**Figure 9d**) (118).

In addition to capture layers, which provide high-affinity binding sites for target analytes, partition layers are also important for quantitative, real-time detection of molecules, such as glucose. Current commercial glucose sensors rely on the user's diligence to take readings from drawn blood in a periodic fashion; as such, data on blood glucose concentration are taken only a few times during the day. A real-time, implantable glucose sensor would be a vast improvement, and SERS may be a route to such a device (4, 87, 119, 120). To develop a viable glucose sensor, researchers must assemble a SERS substrate that allows the glucose to approach the metal surface to benefit from the enhanced EM fields, but also to be rapidly released from the surface to maintain a quantitative equilibrium that accurately reflects the local glucose concentration. This is accomplished using partition layers, which are analogous to the stationary phases used in high-performance liquid chromatography and provide low affinity and rapidly reversible binding sites for target analytes. In the case of glucose sensing, researchers have developed a mixed self-assembled monolayer that has both hydrophobic and hydrophilic components and can assemble on the FON (120). With this functionalized SERS substrate, quantitative detection of local glucose concentration has been demonstrated using SERS both in vitro and in vivo (105, 120). Moreover, the SERS-based glucose sensor measures glucose concentration directly by monitoring its spectral signature, rather than the indirect electrochemical method employed by most commercial sensors. Lastly, this sensor can provide real-time information, allowing potentially harmful fluctuations in glucose levels to be monitored and remedied in a timely manner (120).

All the experiments described thus far detect molecules introduced to the sensing surface via solution-phase chemistry. However, SERS is also an effective means for detecting molecules in the gas phase, as shown in a previous study in which several different molecules were vapor deposited onto a silver FON substrate in ultrahigh vacuum (121). This has recently been expanded to a gas-phase detection protocol under ambient conditions—in particular, for the detection of 2-chloroethyl ethyl sulfide (CEES), a simulant of the chemical-warfare agent mustard gas (122). By incubating a silver FON optimized for 785-nm excitation with CEES-saturated air, researchers observed the Raman spectrum of the CEES molecule, even in the absence of a capture layer. One important feature of this experiment is that they used a portable Raman spectrometer for these measurements; thus, this experiment could be repeated in the field where the presence of chemical-warfare agents must be detected quickly, efficiently, and without false positives. Moreover, CEES could be detected at concentrations much lower than the harmful limit. Thus, this experiment represents an

important first step toward the detection of these harmful gas-phase nerve agents using SERS spectroscopy.

CONCLUSIONS

In this review, we describe studies related both to the fundamental spectroscopic properties of LSPR spectroscopy as well as to several biological and chemical sensing experiments. The results demonstrate the importance of nanoparticle shape and size on both the spectral location of the LSPR and its sensitivity to changes in the local refractive index. Moreover, the response of the nanoparticles is highly distance dependent, as shown with ALD studies measuring both the alumina-induced LSPR shift and the SERS intensity of an adsorbed molecule. Studies in which both the plasmon and Raman excitation wavelength are varied to find the conditions for maximum SERS enhancements demonstrate that the plasmon wavelength should be located somewhere between the excitation and Raman emission wavelengths, as predicted by the EM-enhancement theory. Lastly, localized surface plasmon spectroscopy near molecular resonances provides a new direction for future sensing experiments owing to the enhanced LSPR shifts.

Applications of both wavelength-shift and SERS sensing have shown that a variety of chemically and biologically relevant molecules can be detected—from biomarkers of Alzheimer's disease and anthrax to the direct detection of glucose and chemical-warfare agents. Moreover, the results of these studies demonstrate the necessity of fundamental spectroscopic studies for guiding experimental design to achieve the largest overall signal or to observe signals at all. As our understanding of the plasmonic response of nanoparticles continues to grow, these LSPR-based sensing experiments will improve as well, leading to higher sensitivity, faster and more reversible responses, and an ever-broadening scope of applicability.

SUMMARY POINTS

1. LSPR spectroscopy is used for biological and chemical sensing by transducing changes in the local refractive index via a wavelength-shift measurement.

2. LSPR spectroscopy offers similar sensitivity to the commercially available SPR systems, with the additional advantages of wavelength tunability, smaller sensing volumes, and lower cost instrumentation.

3. Surface-enhanced Raman spectroscopy can identify the presence of specific target molecules based on their unique vibrational signatures. Capture/partition layers provide a means of bringing the target analyte to the nanoparticle surface without obscuring the desired Raman spectrum.

4. Single-nanoparticle LSPR spectroscopy is an important tool for understanding the relationship between local structure and spectra. In addition, single nanoparticles can provide even higher refractive-index sensitivity than nanoparticle arrays.

5. ALD allows the decay of the EM field to be measured as a function of distance from the nanoparticle surface using LSPR wavelength-shift spectroscopy. This same distance dependence can be followed by measuring the SERS enhancement factor of an adsorbed analyte on alumina spacer layers of different thickness.

6. Surface-enhanced Raman spectroscopy is made possible owing to the enhanced EM fields caused by the excitation of plasmon resonances. Fundamental studies of the relationships between the LSPR, the SERS excitation wavelength, and the Raman scattered wavelength reveal that the plasmon resonance wavelength maximum should be positioned between the excitation and Stokes Raman scattered energies. By properly tuning these conditions, enhancement factors up to 10^8 have been recorded for well-defined nanoparticle arrays.

7. LSPR spectroscopy near molecular electronic resonances yields wavelength shifts that are dramatically different than those expected based on a simple refractive-index change. New sensing opportunities arise from this recently discovered effect.

ACKNOWLEDGMENTS

LITERATURE CITED

1. **Jeanmarie DL, Van Duyne RP. 1977. Surface Raman spectroelectrochemistry, part 1: heterocyclic, aromatic, and aliphatic amines adsorbed on the anodized silver electrode. *J. Electroanal. Chem.* 84:1–20**

2. Haynes CL, Yonzon CR, Zhang X. 2005. Surface-enhanced Raman sensors: early history and the development of sensors for quantitative biowarfare agent and glucose detection. *J. Raman Spectrosc.* 36:471–84

3. **Schatz GC, Young MA, Van Duyne RP. 2006. Electromagnetic mechanism of SERS. In *Surface-Enhanced Raman Scattering: Physics and Applications*, ed. K Kneipp, M Moskovits, H Kneipp, pp. 19–46. Berlin: Springer-Verlag**

4. Yonzon CR, Haynes CL, Zhang X, Walsh JT, Van Duyne RP. 2004. A glucose biosensor based on surface-enhanced Raman scattering: improved partition

1. First submitted paper recognizing SERS as a new physical phenomenon with Raman intensity enhancements of 10^5–10^6 (see also Reference 48).

3. Recent chapter describing the important theoretical equations behind the EM-field enhancement responsible for SERS.

layer, temporal stability, reversibility, and resistance to serum protein interference. *Anal. Chem.* 76:78–85

5. Zeman EJ, Schatz GC. 1987. An accurate electromagnetic theory study of surface enhancement factors for silver, gold, copper, lithium, sodium, aluminum, gallium, indium, zinc, and cadmium. *J. Phys. Chem.* 91:634–43

6. Emory SR, Nie S. 1997. Probing single molecules and single nanoparticles by surface-enhanced Raman scattering. *Science* 275:1102–6

7. Kneipp K, Wang Y, Kneipp H, Perelman LT, Itzkan I, et al. 1997. Single molecule detection using surface-enhanced Raman scattering (SERS). *Phys. Rev. Lett.* 78:1667–70

8. Haller KL, Bumm LA, Altkorn RI, Zeman EJ, Schatz GC, Van Duyne RP. 1989. Spatially resolved surface enhanced second harmonic generation: theoretical and experimental evidence for electromagnetic enhancement in the near infrared on a laser microfabricated platinum surface. *J. Chem. Phys.* 90:1237–52

9. Pipino ACR, Schatz GC, Van Duyne RP. 1994. Surface-enhanced second-harmonic diffraction: selective enhancement by spatial harmonics. *Phys. Rev. B* 49:8320–30

10. Pipino ACR, Van Duyne RP, Schatz GC. 1996. Surface-enhanced second-harmonic diffraction: experimental investigation of selective enhancement. *Phys. Rev. B* 53:4162–69

11. Yang W, Hulteen J, Schatz GC, Van Duyne RP. 1996. A surface-enhanced hyper-Raman and surface-enhanced Raman scattering study of *trans*-1,2-bis(4-pyridyl)ethylene adsorbed onto silver film over nanosphere electrodes. Vibrational assignments: experiment and theory. *J. Chem. Phys.* 104:4313–23

12. Geddes CD, Aslan K, Gryczynski I, Malicka J, Lakowicz JR. 2004. Noble-metal surfaces for metal enhanced fluorescence. *Rev. Fluoresc.* 1:365–401

13. Goulet PJG, Aroca RF. 2005. Surface-enhancement of fluorescence near noble metal nanostructures. *Top. Fluoresc. Spectrosc.* 8:223–47

14. Golab JT, Sprague JR, Carron KT, Schatz GC, Van Duyne RP. 1988. A surface-enhanced hyper-Raman scattering study of pyridine adsorbed onto silver: experiment and theory. *J. Chem. Phys.* 88:7942–51

15. Jensen TR, Van Duyne RP, Johnson SA, Maroni VA. 2000. Surface-enhanced infrared spectroscopy: a comparison of metal island films with discrete and nondiscrete surface plasmons. *Appl. Spectrosc.* 54:371–77

16. Shimizu KT, Woo WK, Fisher BR, Eisler HJ, Bawendi MG. 2002. Surface-enhanced emission from single semiconductor nanocrystals. *Phys. Rev. Lett.* 89:117401

17. Haes AJ, Chang L, Klein WL, Van Duyne RP. 2005. Detection of a biomarker for Alzheimer's disease from synthetic and clinical samples using a nanoscale optical biosensor. *J. Am. Chem. Soc.* 127:2264–71

18. Haes AJ, Hall WP, Chang L, Klein WL, Van Duyne RP. 2004. A localized surface plasmon resonance biosensor: first steps toward an assay for Alzheimer's disease. *Nano Lett.* 4:1029–34

19. Haes AJ, Stuart DA, Nie SM, Van Duyne RP. 2004. Using solution-phase nanoparticles, surface-confined nanoparticle arrays and single nanoparticles as biological sensing platforms. *J. Fluoresc.* 14:355–67

6. First paper describing single-molecule SERS using resonant excitation of rhodamine 6G adsorbed on silver nanoparticles (followed independently by Reference 7).

17. First description of a clinical diagnostic procedure using LSPR wavelength-shift sensing.

20. McFarland AD, Van Duyne RP. 2003. Single silver nanoparticles as real-time optical sensors with zeptomole sensitivity. *Nano Lett.* 3:1057–62

21. Yonzon CR, Jeoung E, Zou S, Schatz GC, Mrksich M, Van Duyne RP. 2004. A comparative analysis of localized and propagating surface plasmon resonance sensors: the binding of concanavalin A to a monosaccharide functionalized self-assembled monolayer. *J. Am. Chem. Soc.* 126:12669–76

22. Yonzon CR, Stuart DA, Zhang X, McFarland AD, Haynes CL, Van Duyne RP. 2005. Towards advanced chemical and biological nanosensors: an overview. *Talanta* 67:438–48

23. Yonzon CR, Zhang X, Van Duyne RP. 2003. Localized surface plasmon resonance immunoassay and verification using surface-enhanced Raman spectroscopy. *Proc. SPIE* 5224:78–85

24. Malinsky MD, Kelly KL, Schatz GC, Van Duyne RP. 2001. Chain length dependence and sensing capabilities of the localized surface plasmon resonance of silver nanoparticles chemically modified with alkanethiol self-assembled monolayers. *J. Am. Chem. Soc.* 123:1471–82

25. Jung LS, Campbell CT, Chinowsky TM, Mar MN, Yee SS. 1998. Quantitative interpretation of the response of surface plasmon resonance sensors to adsorbed films. *Langmuir* 14:5636–48

26. Smith EA, Corn RM. 2003. Surface plasmon resonance imaging as a tool to monitor biomolecular interactions in an array based format. *Appl. Spectrosc.* 57:A320–22

27. Brockman JM, Nelson BP, Corn RM. 2000. Surface plasmon resonance imaging measurements of ultrathin organic films. *Annu. Rev. Phys. Chem.* 51:41–63

28. Giebel KF, Bechinger C, Herminghaus S, Riedel M, Leiderer P, et al. 1999. Imaging of cell/substrate contacts of living cells with surface plasmon resonance microscopy. *Biophys. J.* 76:509–16

29. Berger CEH, Beumer TAM, Kooyman RPH, Greve J. 1998. Surface plasmon resonance multisensing. *Anal. Chem.* 70:703–6

30. Endo T, Kerman K, Nagatani N, Takamura Y, Tamiya E. 2005. Label-free detection of peptide nucleic acid-DNA hybridization using localized surface plasmon resonance based optical biosensor. *Anal. Chem.* 77:6976–84

31. Endo T, Yamamura S, Nagatani N, Morita Y, Takamura Y, Tamiya E. 2005. Localized surface plasmon resonance based optical biosensor using surface modified nanoparticle layer for label free monitoring of antigen-antibody reaction. *Sci. Technol. Adv. Mater.* 6:491–500

32. Englebienne P. 1998. Use of colloidal gold surface plasmon resonance peak shift to infer affinity constants from the interactions between protein antigens and antibodies specific for single or multiple epitopes. *Analyst* 123:1599–603

33. Raschke G, Kowarik S, Franzl T, Soennichsen C, Klar TA, et al. 2003. Biomolecular recognition based on single gold nanoparticle light scattering. *Nano Lett.* 3:935–38

34. Srituravanich W, Fang N, Sun C, Luo Q, Zhang X. 2004. Plasmonic nanolithography. *Nano Lett.* 4:1085–88

32. First use of an LSPR wavelength-shift measurement for sensing the local refractive-index change owing to antigen-antibody binding.

33. First report of single-nanoparticle LSPR sensing using single gold nanoparticles (followed independently by Reference 20 using silver nanoparticles).

35. Kik PG, Maier SA, Atwater HA. 2004. Surface plasmons for nanofabrication. *Proc. SPIE* 5347:215–23

36. Sundaramurthy A, Schuck PJ, Conley NR, Fromm DP, Kino GS, Moerner WE. 2006. Toward nanometer-scale optical photolithography: utilizing the near-field of bowtie optical nanoantennas. *Nano Lett.* 6:355–60

37. Malmqvist M. 1993. Biospecific interaction analysis using biosensor technology. *Nature* 361:186–87

38. Van Duyne RP. 2004. Molecular plasmonics. *Science* 306:985–86

39. Knoll W. 1998. Interfaces and thin films as seen by bound electromagnetic waves. *Annu. Rev. Phys. Chem.* 49:569–638

40. Haes AJ, Van Duyne RP. 2004. A unified view of propagating and localized surface plasmon resonance biosensors. *Anal. Bioanal. Chem.* 379:920–30

41. Haes AJ, Haynes CL, McFarland AD, Zou S, Schatz GC, Van Duyne RP. 2005. Plasmonic materials for surface-enhanced sensing and spectroscopy. *MRS Bull.* 30:368–75

42. Zhang X, Young MA, Lyandres O, Van Duyne RP. 2005. Rapid detection of an anthrax biomarker by surface-enhanced Raman spectroscopy. *J. Am. Chem. Soc.* 127:4484–89

43. Kelly KL, Coronado E, Zhao L, Schatz GC. 2003. The optical properties of metal nanoparticles: the influence of size, shape, and dielectric environment. *J. Phys. Chem. B* 107:668–77

44. Knobloch H, Brunner H, Leitner A, Aussenegg F, Knoll W. 1993. Probing the evanescent field of propagating plasmon surface polaritons by fluorescence and Raman spectroscopies. *J. Chem. Phys.* 98:10093–95

45. Miller MM, Lazarides AA. 2005. Sensitivity of metal nanoparticle surface plasmon resonance to the dielectric environment. *J. Phys. Chem. B* 109:21556–65

46. Jensen TR, Duval ML, Kelly L, Lazarides A, Schatz GC, Van Duyne RP. 1999. Nanosphere lithography: effect of the external dielectric medium on the surface plasmon resonance spectrum of a periodic array of silver nanoparticles. *J. Phys. Chem. B* 103:9846–53

47. Hamamoto K, Micheletto R, Oyama M, Umar AA, Kawai S, Kawakami Y. 2006. An original planar multireflection system for sensing using the local surface plasmon resonance of gold nanospheres. *J. Opt. A* 8:268–71

48. Albrecht MG, Creighton JA. 1977. Anomalously intense Raman spectra of pyridine at a silver electrode. *J. Am. Chem. Soc.* 99:5215–17

49. Otto A, Mrozek I, Grabhorn H, Akemann W. 1992. Surface-enhanced Raman scattering. *J. Phys. Condens. Matter* 4:1143–212

50. Moskovits M. 1978. Surface roughness and the enhanced intensity of Raman scattering by molecules adsorbed on metals. *J. Chem. Phys.* 69:4159–61

51. Gersten J, Nitzan A. 1980. Electromagnetic theory of enhanced Raman scattering by molecules adsorbed on rough surfaces. *J. Chem. Phys.* 73:3023–37

52. Metiu H, Das P. 1984. The electromagnetic theory of surface enhanced spectroscopy. *Annu. Rev. Phys. Chem.* 35:507–36

53. Schatz GC. 1984. Theoretical studies of surface enhanced Raman scattering. *Acc. Chem. Res.* 17:370–76

54. Wokaun A. 1985. Surface enhancement of optical fields: mechanism and applications. *Mol. Phys.* 56:1–33

55. Wokaun A. 1984. Surface-enhanced electromagnetic processes. *Solid State Phys.* 38:223–94

56. Haynes CL, Van Duyne RP. 2001. Nanosphere lithography: a versatile nanofabrication tool for studies of size-dependent nanoparticle optics. *J. Phys. Chem. B* 105:5599–611

57. Sherry LJ, Chang SH, Schatz GC, Van Duyne RP, Wiley BJ, Xia Y. 2005. Localized surface plasmon resonance spectroscopy of single silver nanocubes. *Nano Lett.* 5:2034–38

58. Mock JJ, Barbic M, Smith DR, Schultz DA, Schultz S. 2002. Shape effects in plasmon resonance of individual colloidal silver nanoparticles. *J. Chem. Phys.* 116:6755–59

59. Haynes CL, McFarland AD, Smith MT, Hulteen JC, Van Duyne RP. 2002. Angle-resolved nanosphere lithography: manipulation of nanoparticle size, shape, and interparticle spacing. *J. Phys. Chem. B* 106:1898–902

60. Haynes CL, McFarland AD, Van Duyne RP. 2005. Surface-enhanced Raman spectroscopy. *Anal. Chem.* 77:A338–46

61. Moran AM, Sung J, Hicks EM, Van Duyne RP, Spears KG. 2005. Second harmonic excitation spectroscopy of silver nanoparticle arrays. *J. Phys. Chem. B* 109:4501–6

62. Whitney AV, Elam JW, Zou S, Zinovev AV, Stair PC, et al. 2005. Localized surface plasmon resonance nanosensor: a high-resolution distance-dependence study using atomic layer deposition. *J. Phys. Chem. B* 109:20522–28

63. Haes AJ, Zou S, Schatz GC, Van Duyne RP. 2004. A nanoscale optical biosensor: the long range distance dependence of the localized surface plasmon resonance of noble metal nanoparticles. *J. Phys. Chem. B* 108:109–16

64. Nehl CL, Liao H, Hafner JH. 2006. Optical properties of star-shaped gold nanoparticles. *Nano Lett.* 6:683–88

65. Xia Y, Halas NJ. 2005. Shape-controlled synthesis and surface plasmonic properties of metallic nanostructures. *MRS Bull.* 30:338–48

66. Wiley B, Sun Y, Mayers B, Xia Y. 2005. Shape-controlled synthesis of metal nanostructures: the case of silver. *Chem. A Eur. J.* 11:454–63

67. Sun Y, Xia Y. 2002. Shape-controlled synthesis of gold and silver nanoparticles. *Science* 298:2176–79

68. Zhang X, Hicks EM, Zhao J, Schatz GC, Van Duyne RP. 2005. Electrochemical tuning of silver nanoparticles fabricated by nanosphere lithography. *Nano Lett.* 5:1503–7

69. Jin R, Cao YC, Hao E, Metraux GS, Schatz GC, Mirkin CA. 2003. Controlling anisotropic nanoparticle growth through plasmon excitation. *Nature* 425:487–90

70. Jin R, Cao Y, Mirkin CA, Kelly KL, Schatz GC, Zheng JG. 2001. Photoinduced conversion of silver nanospheres to nanoprisms. *Science* 294:1901–3

71. Haynes CL, McFarland AD, Zhao L, Van Duyne RP, Schatz GC, et al. 2003. Nanoparticle optics: the importance of radiative dipole coupling in two-dimensional nanoparticle arrays. *J. Phys. Chem. B* 107:7337–42

72. Athawale AA, Katre PP, Majumdar MB. 2005. Nonaqueous phase synthesis of copper nanoparticles. *J. Nanosci. Nanotech.* 5:991–93

73. Bohren CF, Huffman DR. 1983. *Absorption and Scattering of Light by Small Particles.* New York: Wiley. 530 pp.

74. Mie G. 1908. Contributions to the optics of turbid media, especially colloidal metal solutions. *Ann. Phys.* 25:377–445

75. Link S, El-Sayed MA. 1999. Spectral properties and relaxation dynamics of surface plasmon electronic oscillations in gold and silver nano-dots and nano-rods. *J. Phys. Chem. B* 103:8410–26

76. Draine BT, Flatau PJ. 1994. Discrete-dipole approximation for scattering calculations. *J. Opt. Soc. Am. A* 11:1491–99

77. Jensen TR, Kelly KL, Lazarides A, Schatz GC. 1999. Electrodynamics of noble metal nanoparticles and nanoparticle clusters. *J. Cluster Sci.* 10:295–317

78. Yang W, Schatz GC, Van Duyne RP. 1995. Discrete dipole approximation for calculating extinction and Raman intensities for small particles with arbitrary shapes. *J. Chem. Phys.* 103:869–75

79. Novotny L, Bian RX, Xie XS. 1997. Theory of nanometric optical tweezers. *Phys. Rev. Lett.* 79:645–48

80. Bian RX, Dunn RC, Xie XS, Leung PT. 1995. Single molecule emission characteristics in near-field microscopy. *Phys. Rev. Lett.* 75:4772–75

81. Taflove A. 1995. *Computational Electrodynamics: The Finite-Difference Time Domain Method.* Boston: Artech House

82. Haes AJ, Van Duyne RP. 2002. A nanoscale optical biosensor: sensitivity and selectivity of an approach based on the localized surface plasmon resonance of triangular silver nanoparticles. *J. Am. Chem. Soc.* 124:10596–604

83. Van Duyne RP. 1979. Laser excitation of Raman scattering from adsorbed molecules on electrode surfaces. *Chem. Biochem. Appl. Lasers* 4:101–85

84. McFarland AD, Young MA, Dieringer JA, Van Duyne RP. 2005. Wavelength-scanned surface-enhanced Raman excitation spectroscopy. *J. Phys. Chem. B* 109:11279–85

85. Haynes CL, Haes AJ, Van Duyne RP. 2001. Nanosphere lithography: synthesis and application of nanoparticles with inherently anisotropic structures and surface chemistry. In *Anisotropic Nanoparticles: Synthesis, Characterization, Applications,* ed. LA Lyon, S Stranick, CD Keating, P Searson, pp. C.6.3.1–6.3. Warrendale, PA: MRS

86. Hulteen JC, Van Duyne RP. 1995. Nanosphere lithography: a materials general fabrication process for periodic particle array surfaces. *J. Vac. Sci. Technol. A* 13:1553–58

87. Stuart DA, Yonzon CR, Zhang X, Lyandres O, Shah NC, et al. 2005. Glucose sensing using near-infrared surface-enhanced Raman spectroscopy: gold surfaces, 10-day stability, and improved accuracy. *Anal. Chem.* 77:4013–19

88. Hicks EM, Zhang XY, Zou SL, Lyandres O, Spears KG, et al. 2005. Plasmonic properties of film over nanowell surface fabricated by nanosphere lithography. *J. Phys. Chem. B* 109:22351–58

75. Excellent review article on the size-dependent spectral properties of gold nanoparticles.

83. Earliest appearance of the term surface-enhanced Raman spectroscopy and the acronym SERS in print.

84. Extensive study of the relationship between the SERS excitation spectrum and the LSPR spectrum of the enhancing substrate.

86. Introduces the concept of NSL as a low-cost, materials general nanofabrication technique.

89. Hicks EM, Zou S, Schatz GC, Spears KG, Van Duyne RP, et al. 2005. Controlling plasmon line shapes through diffractive coupling in linear arrays of cylindrical nanoparticles fabricated by electron beam lithography. *Nano Lett.* 5:1065–70

90. Lamprecht B, Schider G, Lechner RT, Ditlbacher H, Krenn JR, et al. 2000. Metal nanoparticle gratings: influence of dipolar particle interaction on the plasmon resonance. *Phys. Rev. Lett.* 84:4721–24

91. Fromm DP, Sundaramurthy A, Schuck PJ, Kino G, Moerner WE. 2004. Gap-dependent optical coupling of single "bowtie" nanoantennas resonant in the visible. *Nano Lett.* 4:957–61

92. Wiley B, Sun Y, Xia Y. 2005. Polyol synthesis of silver nanostructures: control of product morphology with Fe(II) or Fe(III) species. *Langmuir* 21:8077–80

93. Im Sang H, Lee Yun T, Wiley B, Xia Y. 2005. Large-scale synthesis of silver nanocubes: the role of HCl in promoting cube perfection and monodispersity. *Angew. Chem.* 44:2154–57

94. Jun Y, Choi J, Cheon J. 2006. Shape control of semiconductor and metal oxide nanocrystals through nonhydrolytic colloidal routes. *Angew. Chem.* 45:3414–39

95. Xu Q, Bao J, Capasso F, Whitesides GM. 2006. Surface plasmon resonances of free-standing gold nanowires fabricated by nanoskiving. *Angew. Chem.* 45:3631–35

96. Haes AJ, Zhao J, Zou S, Own CS, Marks LD, et al. 2005. Solution-phase, triangular Ag nanotriangles fabricated by nanosphere lithography. *J. Phys. Chem. B* 109:11158–62

97. Jensen TR, Malinsky MD, Haynes CL, Van Duyne RP. 2000. Nanosphere lithography: tunable localized surface plasmon resonance spectra of silver nanoparticles. *J. Phys. Chem. B* 104:10549–56

98. Mock JJ, Smith DR, Schultz S. 2003. Local refractive index dependence of plasmon resonance spectra from individual nanoparticles. *Nano Lett.* 3:485–91

99. Michaels AM, Nirmal M, Brus LE. 1999. Surface enhanced Raman spectroscopy of individual rhodamine 6G molecules on large Ag nanocrystals. *J. Am. Chem. Soc.* 121:9932–39

100. Sherry LJ, Jin R, Mirkin CA, Schatz GC, Van Duyne RP. 2006. Localized surface plasmon resonance spectroscopy of single silver triangular nanoprisms. *Nano Lett.* In press

101. Haes AJ, Zou S, Schatz GC, Van Duyne RP. 2004. A nanoscale optical biosensor: the short range distance dependence of the localized surface plasmon resonance of silver and gold nanoparticles. *J. Phys. Chem. B* 108:6961–68

102. Groner MD, Elam JW, Fabreguette FH, George SM. 2002. Electrical characterization of thin Al_2O_3 films grown by atomic layer deposition on silicon and various metal substrates. *Thin Solid Films* 413:186–97

103. Ritala M, Leskela M. 2002. Atomic layer deposition. In *Handbook of Thin Film Materials*, ed. HS Nalwa, Vol. 1, pp. 103–59. San Diego: Academic

104. Ott AW, Klaus JW, Johnson JM, George SM. 1997. Al_2O_3 thin film growth on Si(100) using binary reaction sequence chemistry. *Thin Solid Films* 292:135–44

105. Dieringer JA, McFarland AD, Shah NC, Stuart DA, Whitney AV, et al. 2005. Surface enhanced Raman spectroscopy: new materials, concepts, characterization tools, and applications. *Faraday Discuss.* 132:9–26

106. Kennedy BJ, Spaeth S, Dickey M, Carron KT. 1999. Determination of the distance dependence and experimental effects for modified SERS substrates based on self-assembled monolayers formed using alkanethiols. *J. Phys. Chem. B* 103:3640–46

107. Haynes CL, Van Duyne RP. 2003. Plasmon-sampled surface-enhanced Raman excitation spectroscopy. *J. Phys. Chem. B* 107:7426–33

108. Zou S, Schatz GC. 2005. Silver nanoparticle array structures that produce giant enhancements in electromagnetic fields. *Chem. Phys. Lett.* 403:62–67

109. Haes AJ, Zou S, Zhao J, Schatz GC, Van Duyne RP. 2006. Localized surface plasmon resonance spectroscopy near molecular resonances. *J. Am. Chem. Soc.* 128:10905–14

110. Reinhard BM, Siu M, Agarwal H, Alivisatos AP, Liphardt J. 2005. Calibration of dynamic molecular rulers based on plasmon coupling between gold nanoparticles. *Nano Lett.* 5:2246–52

111. Soennichsen C, Reinhard BM, Liphardt J, Alivisatos AP. 2005. A molecular ruler based on plasmon coupling of single gold and silver nanoparticles. *Nat. Biotech.* 23:741–45

112. Riboh JC, Haes AJ, McFarland AD, Yonzon CR, Van Duyne RP. 2003. A nanoscale optical biosensor: real-time immunoassay in physiological buffer enabled by improved nanoparticle adhesion. *J. Phys. Chem. B* 107:1772–80

113. Gong Y, Chang L, Viola KL, Lacor PN, Lambert MP, et al. 2003. Alzheimer's disease-affected brain: presence of oligomeric AB ligands (ADDLs) suggests a molecular basis for reversible memory loss. *Proc. Natl. Acad. Sci. USA* 100:10417–22

114. Lambert MP, Barlow AK, Chromy BA, Edwards C, Freed R, et al. 1998. Diffusible, nonfibrillar ligands derived from $A\beta_{1-42}$ are potent central nervous system neurotoxins. *Proc. Natl. Acad. Sci. USA* 95:6448–53

115. Lambert MP, Viola KL, Chromy BA, Chang L, Morgan TE, et al. 2001. Vaccination with soluble $A\beta$ oligomers generates toxicity-neutralizing antibodies. *J. Neurochem.* 79:595–605

116. Chapman SC, Kenny HA, Woodruff TK. 2004. Activin, inhibin, and follistatin in ovarian physiology. In *The Ovary*, ed. PCK Leung, EY Adashi, pp. 273–87. San Diego: Elsevier

117. Zhao J, Das A, Zhang X, Schatz GC, Sligar SG, Van Duyne RP. 2006. Resonance surface plasmon spectroscopy: low molecular weight substrate binding to cytochrome P450. 128:11004–5

118. Zhang X, Zhao J, Whitney AV, Elam JW, Van Duyne RP. 2006. Ultrastable substrates for surface-enhanced Raman spectroscopy: Al_2O_3 overlayers fabricated by atomic layer deposition yield improved anthrax biomarker detection. *J. Am. Chem. Soc.* 128:10304–9

119. Shafer-Peltier KE, Haynes CL, Glucksberg MR, Van Duyne RP. 2003. Toward a glucose biosensor based on surface-enhanced Raman scattering. *J. Am. Chem. Soc.* 125:588–93

120. Lyandres O, Shah NC, Yonzon CR, Walsh JT, Glucksberg MR, Van Duyne RP. 2005. Real-time glucose sensing by surface-enhanced Raman spectroscopy in bovine plasma facilitated by a mixed decanethiol/mercaptohexanol partition layer. *Anal. Chem.* 77:6134–39

121. Litorja M, Haynes CL, Haes AJ, Jensen TR, Van Duyne RP. 2001. Surface-enhanced Raman scattering detected temperature programmed desorption: optical properties, nanostructure, and stability of silver film over SiO_2 nanosphere surfaces. *J. Phys. Chem. B* 105:6907–15

122. Stuart DA, Biggs KB, Van Duyne RP. 2006. Surface-enhanced Raman spectroscopy of half-mustard agent. *Analyst* 131:568–72

Contents